01 Jan 2022

Direct Numerical Simulation of Acoustic Disturbances in a Hypersonic Two-Dimensional Nozzle Configuration

Nathaniel Hildebrand

Meelan M. Choudhari

Cole P. Deegan

Junji Huang

et. al. For a complete list of authors, see https://scholarsmine.mst.edu/mec_aereng_facwork/4965

Recommended Citation

N. Hildebrand et al., "Direct Numerical Simulation of Acoustic Disturbances in a Hypersonic Two-Dimensional Nozzle Configuration," *AIAA Journal*, vol. 60, no. 6, pp. 3452 - 3463, American Institute of Aeronautics and Astronautics, Jan 2022.
The definitive version is available at https://doi.org/10.2514/1.J061053

AIAA JOURNAL
Vol. 60, No. 6, June 2022

Direct Numerical Simulation of Acoustic Disturbances in a Hypersonic Two-Dimensional Nozzle Configuration

Nathaniel Hildebrand* and Meelan M. Choudhari†
NASA Langley Research Center, Hampton, Virginia 23681
Cole P. Deegan‡
Missouri University of Science and Technology, Rolla, Missouri 65409
and
Junji Huang§ and Lian Duan¶
The Ohio State University, Columbus, Ohio 43210

https://doi.org/10.2514/1.J061053

Direct numerical simulations (DNS) are performed to study acoustic radiation in a quasi-two-dimensional nozzle with two independent spatially evolving turbulent boundary layers with an edge Mach number of 6. The emphasis of this work is to compare the radiated pressure fluctuations in a geometrically confined environment with those radiated from a single wall in an unconfined setting. The boundary-layer profile of the rms pressure fluctuation scaled by the mean shear stress at the wall is found to be in good agreement with prior flat-plate calculations at similar conditions. However, the normalized rms pressure fluctuation within the freestream region is significantly higher than that in the unconfined case, by a factor that is approximately equal to $\sqrt{2}$. The application of two different compressibility transformations to the computed mean velocity profiles indicates that, in comparison with the van Driest transformation, the Trettel and Larsson transformation provides a better collapse with flat-plate simulations over a broad range of Mach numbers. The DNS data also reveal that, in spite of displaying a strongly non-Gaussian behavior inside the boundary layer, the radiated acoustic fluctuations in all thermodynamic variables have a skewness of approximately 0.3, indicating a minor deviation with respect to Gaussian behavior. Surface pressure fluctuations along the nozzle walls are not significantly impacted by the acoustic waves radiating from the opposite wall.

Nomenclature

a	=	speed of sound, m/s
C_f	=	skin-friction coefficient, dimensionless
C_{pp}	=	two-point correlation coefficient field, dimensionless
c_p	=	coefficient of specific heat at constant pressure, $\text{J}/(\text{K}\cdot\text{kg})$
H	=	shape factor defined as δ^*/θ, dimensionless
L	=	length of domain, m
M	=	Mach number, dimensionless
N	=	number of grid points, dimensionless
Pr	=	Prandtl number, dimensionless
p	=	pressure, Pa
R	=	ideal gas constant, $\text{J}/(\text{K}\cdot\text{kg})$
Re_{δ^*}	=	Reynolds number based on displacement thickness defined as $\rho_\infty U_\infty \delta^*/\mu_\infty$, dimensionless
Re_θ	=	Reynolds number based on momentum thickness defined as $\rho_\infty U_\infty \theta/\mu_\infty$, dimensionless
Re_τ	=	Reynolds number based on shear velocity and wall viscosity defined as $\rho_w u_\tau \delta/\mu_w$, dimensionless
T	=	temperature, K
T_r	=	recovery temperature defined as $T_\infty[1+0.45(\gamma-1)M_\infty^2]$, K
T_s	=	Sutherland's temperature, K
t	=	time, s
unit Re	=	unit Reynolds number defined as $\rho_\infty U_\infty/\mu_\infty$, $1/\text{m}$
(u, v, w)	=	streamwise, spanwise, and wall-normal velocity components, m/s
(x, y, z)	=	Cartesian coordinates, m
z_n	=	wall-normal distance, m
z_τ	=	viscous length defined as ν_w/u_τ, m
γ	=	specific-heat ratio defined as c_p/c_v, dimensionless
δ	=	boundary-layer thickness, m
δ^*	=	boundary-layer displacement thickness, m
θ	=	boundary-layer momentum thickness, m
κ	=	coefficient of thermal conductivity, $\text{W}/(\text{m}\cdot\text{K})$
μ	=	dynamic viscosity, $\text{kg}/(\text{m}\cdot\text{s})$
ρ	=	density, kg/m^3
Φ	=	power spectral density amplitude, Pa^2/Hz

Subscripts

M	=	Morkovin transform
rms	=	root mean square
TL	=	Trettel and Larsson transform
VD	=	van Driest transform
w	=	wall variable
∞	=	freestream variable

Superscripts

$''$	=	fluctuations around density-weighted (Favre) averages
$'$	=	fluctuations around standard (Reynolds) averages
$*$	=	semilocal unit
$+$	=	viscous unit based on conditions at streamwise location of interest

Received 6 July 2021; revision received 17 December 2021; accepted for publication 6 January 2022; published online 28 February 2022.

*Aerospace Technologist, Computational AeroSciences Branch. Member AIAA.
†Aerospace Technologist, Computational AeroSciences Branch. Fellow AIAA.
‡Graduate Student, Mechanical and Aerospace Engineering Department; currently Product Engineer, Honeywell Federal Manufacturing and Technologies, Kansas City, MO. Student Member AIAA.
§Graduate Student, Mechanical and Aerospace Engineering Department. Student Member AIAA.
¶Associate Professor, Mechanical and Aerospace Engineering Department. Associate Fellow AIAA.

I. Introduction

TRANSITION from laminar to turbulent flow in a high-speed boundary layer results in a sizable increase of the skin-friction drag and heat flux. Uncertainties in transition prediction can have a substantial impact on the design and performance of a hypersonic vehicle, including weight, structure, and engine operability [1]. At flight altitudes, transition is often initiated by linear instabilities of the boundary-layer flow, which are excited via the receptivity of this flow to its disturbance environment. Aerothermodynamic testing of high-speed vehicles usually occurs in conventional or noisy wind-tunnel facilities even though experimental measurements show these wind tunnels produce an earlier onset of transition when compared to a flight environment [2]. Low-disturbance (i.e., quiet) wind tunnels mimic the in-flight transition characteristics, but they are limited in size, Mach number, maximum freestream enthalpy, and quiet-flow Reynolds number. Therefore, we need to better understand the disturbance environment in a noisy high-speed wind tunnel, which consists of acoustic, vortical, and entropy waves, along with particulates from the incoming flow.

Acoustic disturbances arise from turbulent eddies in the high-speed boundary layers that develop along the wind-tunnel nozzle walls [3], and as the freestream Mach number increases, the intensity of these acoustic disturbances becomes much stronger. Therefore, acoustic disturbances usually dominate the overall disturbance environment (as opposed to vorticity or entropy disturbances) at Mach numbers of 2.5 or higher [4–7]. We focus our attention on modeling and understanding these acoustic disturbances to allow for a better use of the high-speed transition data from conventional or noisy facilities. Also, with an increased knowledge base of the different receptivity mechanisms in high-speed boundary layers [8,9], it becomes more important to characterize the details of this acoustic field so that the receptivity theories may be applied to transition prediction in conventional wind tunnels. This characterization would also help with the process of extrapolating wind-tunnel measurements to flight tests.

Direct numerical simulations (DNS) provide access to flow variables that cannot be easily measured [2,10] and can either solve or bypass many other difficulties associated with experiments. Recent work [11–14] has successfully used DNS to capture acoustic disturbances radiating from high-speed turbulent boundary layers (TBLs) over a flat plate at Mach numbers ranging from 2.5 to 14. These simulations isolated the acoustic radiation from a single surface, hence facilitating a comprehensive understanding of the overall disturbance environment and its dependence on certain boundary-layer parameters (such as edge Mach number, wall temperature, and local Reynolds number). Direct numerical simulation has also been used to investigate acoustic radiation from TBLs developing along the inner walls of an axisymmetric nozzle [15] and a two-dimensional (2-D) channel [16,17]. A more recent study [18] used DNS to assess the impact of favorable pressure gradients due to streamline curvature on a Mach 4.9 TBL.

There are several conventional hypersonic wind-tunnel facilities that have a rectangular test section. One such facility is the NASA 20-Inch Mach 6 Wind Tunnel [19]. It is important to point out that nonaxisymmetric wind tunnels have freestream disturbances that represent the net effect of acoustic radiation from the boundary layers along the four nozzle walls and the corner flows in between them. The spatiotemporal characteristics of freestream disturbances in a rectangular test section are determined by the outcome of acoustic reverberation within the confined environment, and the nature of this reverberation in a nonaxisymmetric nozzle is expected to be different from that inside an axisymmetric wind tunnel. Our current research effort summarizes and expands on the earlier works by Deegan et al. [20] and Hildebrand et al. [21], which presented simulations of the acoustic radiation in a quasi-2-D nozzle (similar to the convergent–divergent nozzle from the NASA 20-Inch Mach 6 Wind Tunnel, but without the two spanwise end walls). The current work will characterize the hydrodynamic statistics in a hypersonic TBL over a tunnel wall with mild streamwise curvature, investigate the dependence of intensity and power spectral density of the freestream noise on the number of TBLs, examine the influence of freestream noise on the wall pressure fluctuations, and describe the spatial structures.

By diminishing the significant impact of the spanwise end walls and the corners in between them on the acoustic noise generation and reverberation processes, the simpler quasi-2-D flow configuration provides a useful reference toward characterizing the effects of the individual wind-tunnel nozzle walls on the disturbance environment. From a strictly numerical standpoint, it provides a less expensive means of fine-tuning the simulation process for the eventual fully three-dimensional (3-D) simulation that includes the nozzle end walls, and hence will enable comparisons with the experiments performed in the NASA 20-Inch Mach 6 Wind Tunnel [19].

This paper is structured in the following manner. Section II discusses the flow configuration in detail. The governing equations and numerical methods are described in Sec. III. Results from the DNS are presented in Sec. IV, which includes comparisons with past simulations while addressing the relative effects of having one or two spatially evolving turbulent nozzle-wall boundary layers that radiate noise. We conclude this paper in Sec. V with remarks and the outlook for future research directions, including the fully 3-D simulation with nozzle end walls.

II. Flow Configuration

In this work, we simulate turbulent high-speed flow in a quasi-2-D configuration of a rectangular nozzle test section. Quasi-2-D refers to the fact that instead of modeling the spanwise end walls, we employ a finite width spanwise domain with periodic boundary conditions. Reynolds-averaged Navier–Stokes (RANS) equations are used to simulate the converging and diverging nozzle test sections (refer to Ref. [20] for details), whereas DNS is used only to simulate the diverging section of the wind-tunnel nozzle. Because the nozzle cross section is rectangular, there is no curvature in the spanwise direction, and hence, it is nonaxisymmetric. Figure 1 depicts a slice along the midspan location from the DNS solution, indicating the contours of time-averaged Mach number and temperature. The computational domain for the DNS starts at $x = 0.305$ m (i.e., slightly downstream of the nozzle throat) and extends to the nozzle exit at $x = 3.67$ m. This domain size captures the acoustic sources responsible for generating the freestream noise inside the nozzle test section. Additional runs were performed with the inflow at a farther downstream location of $x = 0.436$ m, and the resulting statistics were practically the same as those based on the current inflow location of $x = 0.305$ m, confirming the insensitivity of our DNS results to the selected inflow location (refer to Hildebrand et al. [21]).

The flow conditions in this work are based on the operating range of the NASA 20-Inch Mach 6 Wind Tunnel. We set the unit Reynolds number in this simulation to 7.3×10^6 (1/m). The freestream Mach number, velocity, temperature, and density are $M_\infty = 5.97$, $u_\infty = 948$ m/s, $T_\infty = 64.3$ K, and $\rho_\infty = 0.033$ kg/m^3, respectively. These freestream values are the exact same as those reported in our two prior studies [20,21]. In these two prior studies [20,21], we misreported the unit Reynolds number as 2×10^6 (1/m), which should be 7.3×10^6 (1/m) based on the specified freestream values. Here, *freestream* refers to the center or $z = 0$ m of the outflow station at $x = 3.67$ m. The wall temperature is 300 K, which corresponds to a wall-to-recovery-temperature ratio of $T_w/T_r \approx 0.63$. Refer to Table 1 for the boundary-layer properties of the different simulations. The first row in Table 1 corresponds to results from Pate's correlation [6]. We use Cartesian coordinates with x, y, and z denoting the streamwise, spanwise, and wall-normal directions, respectively.

Two different grids are used for the DNS to show convergence of the computed acoustic characteristics. One is denoted as the baseline grid [20], whereas the other is denoted as the refined grid [21] for simplicity. Table 2 shows the various grid properties. The refined grid has much smaller values of x^+ and z^+ than the baseline grid, particularly from $x = 0.5$ m to $x = 2.5$ m (refer to Ref. [21]). Because a portion of the acoustic fluctuations in the downstream region of interest may have been generated in the upstream regions where the boundary layer is relatively thinner, it is important to assess the effect of a finer wall-normal spacing on the acoustic fluctuations in the test

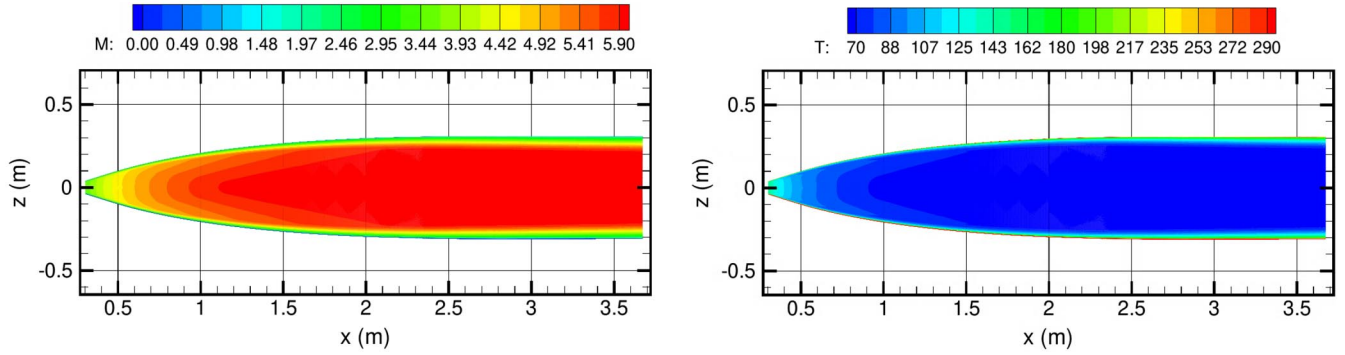

a) Contours of Mach number on a spanwise slice **b) Contours of temperature on a spanwise slice**

Fig. 1 Contours of time-averaged a) Mach number and b) temperature from the DNS of Mach 6 flow in a rectangular nozzle test section; due to sensitivity of the nozzle geometry, for the purpose of this illustration, the nozzle shape has been nonuniformly distorted from its actual contour.

section. In the spanwise direction, we employ a constant grid spacing with a value of $y^+ = 5.39$. A total of $N_x = 5630$, $N_y = 400$, and $N_z = 1199$ grid points resolve the computational domain in the streamwise, spanwise, and wall-normal directions, respectively, for the refined grid. We append a fringe zone to the outflow boundary with a mesh that becomes more stretched in the streamwise direction to minimize acoustic reflections from the downstream boundary. Moreover, the spanwise domain width is 0.1485 m. This value is approximately 30% of the actual tunnel width. It is also more than twice the boundary-layer thickness at $x = 3.3$ m (i.e., the region of interest where the various statistics have been calculated).

III. Governing Equations and Numerical Methods

The computational domain for the DNS extends across a majority of the diverging section of the tunnel nozzle. The inflow conditions for the DNS are based on the solution to the RANS equations that models one quarter of the rectangular nozzle geometry along both converging and diverging segments of the nozzle contour. To solve the RANS equations, we employ the Viscous Upwind Algorithm for Complex Flow Analysis software [22], which is based on Menter's shear stress transport turbulence model [23]. This software numerically solves the unsteady conservation equations for calorically or thermally perfect gases with a spatially second-order-accurate cell-centered finite volume method. The inviscid fluxes are constructed using the MUSCL $\kappa = 0$ scheme in conjunction with the low-dissipation flux-split scheme of Edwards [24]. No gradient limiter is used in these computations. Furthermore, the cell–face gradients required to construct the viscous fluxes are obtained using an auxiliary control-volume approach that results in a compact viscous stencil, which produces a second-order-accurate approximation of the full Navier–Stokes viscous fluxes. Further, the solutions are relaxed in pseudotime to steady state using the 3-D ILU(0) scheme [22] with a constant Courant–Friedrichs–Lewy number on the order of 25.

For the DNS, the compressible three-dimensional Navier–Stokes equations in conservative form are solved numerically in curvilinear coordinates. They describe the spatiotemporal evolution of the system state and can be written in the form

$$\frac{\partial \boldsymbol{U}}{\partial t} + \frac{\partial \boldsymbol{F}}{\partial \xi} + \frac{\partial \boldsymbol{G}}{\partial \eta} + \frac{\partial \boldsymbol{H}}{\partial \zeta} = 0 \tag{1}$$

where $\boldsymbol{U} = [\rho, \rho u, \rho v, \rho w, \rho e]^T$ is the vector of conserved solution variables, and $\boldsymbol{F} = \boldsymbol{F}_c + \boldsymbol{F}_v$ is the flux vector consisting of both inviscid and viscous components ($\boldsymbol{G}$ and $\boldsymbol{H}$ are similar to $\boldsymbol{F}$). The inviscid fluxes are computed using a seventh-order weighted essentially nonoscillatory (WENO) scheme with limiters [25] to reduce numerical dissipation. The WENO adaption is limited to the boundary-layer region to maintain numerical stability. The optimal stencil of the WENO scheme is employed outside the boundary layer to achieve a higher resolution of the radiated acoustic field. We discretize the viscous fluxes using a central fourth-order finite difference scheme. Time integration is performed with a third-order low-storage Runge–Kutta scheme [26]. Refer to Wu and Martín [27] for more details regarding the governing equations.

We assume the fluid is a perfect gas and the usual constitutive relations for a Newtonian fluid hold: the viscous-stress tensor is linearly related to the rate-of-strain tensor, and the heat-flux vector is linearly related to the temperature gradient through Fourier's law. The density ρ and temperature T are related to the pressure p through the equation of state $p = \rho RT$, where $R = 287.15$ J/(kg · K) is the specific gas constant for air. We compute the dynamic viscosity μ from Sutherland's law as such $\mu(T) = c_1 T^{1.5}/(T + T_s)$. The constants in Sutherland's law are set to the values of $c_1 = 1.458 \times 10^{-6}$ kg/(ms · $\sqrt{\text{K}}$) and $T_s = 110.4$ K. Furthermore, the Prandtl number is set to $Pr = \mu c_p/\kappa = 0.71$, where c_p and κ are the coefficients of specific heat at constant pressure and thermal conductivity, respectively. We

Table 1 Boundary-layer properties at the nozzle exit ($x = 3.67$ m)

Case	M_∞	Unit Re, 1/m	T_w, K	T_w/T_r	Re_τ	δ, mm	δ^*, mm	H	z_τ, μm	C_f, 10^{-3}
Pate	5.97	7.3×10^6	300	0.63	1343	70.8	37.0	12.0	52.7	1.13
RANS	5.98	7.3×10^6	300	0.63	995.4	68.4	32.1	7.7	68.8	0.79
DNS	5.97	7.3×10^6	300	0.63	990.5	68.9	27.3	6.7	69.5	0.78

Table 2 Domain and grid resolution parameters for the baseline [20] and refined [21] simulations

Grid	x_{in}, m	x_{out}, m	L_x, m	N_x	N_y	N_z	x^+_{min}	y^+	z^+_w	z^+_∞	L_x/δ_r
Baseline	0.305	3.67	3.27	4000	400	1199	11.61	5.39	1.07	7.44	47.8
Refined	0.305	3.67	3.27	5630	400	1199	10.43	5.39	0.98	3.27	47.8

define the Mach number as $M = U/a$, where $a = \sqrt{\gamma p/\rho}$ is the speed of sound. Further, the constant ratio of specific heats is set to a constant value of $\gamma = 1.4$.

For the inflow boundary condition of the DNS, a digital-filter-based synthetic turbulence injection method is applied that generates correlated random fluctuations on nonuniform curvilinear meshes [28,29]. The digital filtering method has previously been validated against the recycling method and other reference data [30]. The mean profiles, integral lengths, and Reynolds-stress tensor required for the digital filter are obtained from the precursor RANS computation that simulates the full wind-tunnel geometry [20]. No-slip boundary conditions are enforced for the three velocity components (streamwise, wall normal, and spanwise) along the walls. Note that no symmetry condition is being imposed along the nozzle centerline, and the simulation is capable of capturing the reverberating character of the acoustic disturbance environment within the quasi-2-D nozzle. An isothermal wall boundary condition is used for the temperature. An unsteady nonreflecting boundary condition based on Thompson [31] is used at the outflow boundary of the computational domain, in conjunction with a fringe zone to minimize acoustic reflections from the downstream boundary. Lastly, periodic boundary conditions are employed in the spanwise direction.

IV. Results

The simpler quasi-2-D flow configuration allows for a characterization of the most rudimentary effects of the individual wind-tunnel walls on the overall acoustic disturbance field within the wind tunnel. It also provides a less expensive way to refine and tune the simulation process for the eventual fully 3-D simulation that includes the end walls. In this section, we compare the DNS results on two different grids, employ two different velocity transformations, examine the high-order turbulent statistics, characterize the various pressure spectra, show instantaneous snapshots from the DNS, and plot bidirectional correlation coefficients. We also compare results from our quasi-2-D flow configuration to published data for turbulent flat-plate boundary layers in an unconfined environment away from the plate.

A. Hydrodynamic Characteristics

To help establish the accuracy of our DNS data, we begin with a comparison of the DNS results obtained for two separate grids with different mesh resolutions, as described in Refs. [20,21], respectively. The time-averaged DNS solution for the refined grid is computed by using 150 instantaneous snapshots with a time interval of 5.3×10^{-5} s between each successive pair of snapshots. Figure 2 shows the Mach-number distribution along the nozzle axis for the RANS solution, for computations based on a one-dimensional (1-D) isentropic approximation, and for the two DNS solutions with different grids. There is excellent agreement between the RANS and both

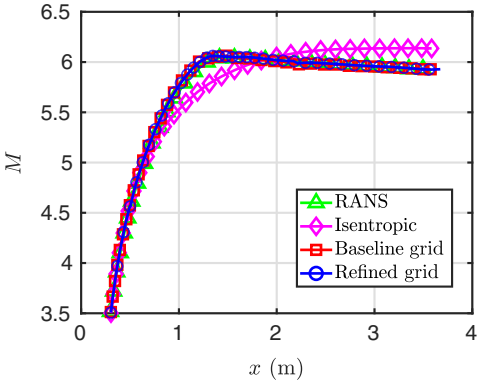

Fig. 2 Comparison of the centerline Mach number (at $z = 0$ m) obtained from the RANS solution, 1-D isentropic approximation, and two DNS solutions with different grids.

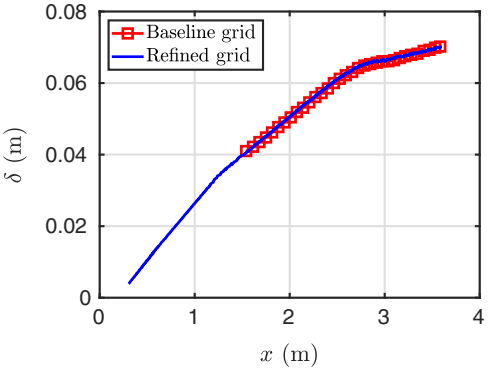

Fig. 3 Comparison between two DNS solutions with different grid resolutions in terms of the streamwise evolution of boundary-layer thickness along the bottom wall.

DNS solutions in terms of centerline Mach number. Both the RANS and time-averaged DNS solutions depart from the 1-D isentropic approximation after $x = 0.75$ m. Figure 3 depicts a comparison of the streamwise variation in boundary-layer thickness along the bottom wall for the DNS solutions obtained with the baseline and refined grids. One may observe that the boundary-layer thickness distributions for the two DNS solutions match very well with each other.

Figure 4 shows a comparison between the Mach-number profiles from RANS and DNS solutions at three selected streamwise locations ($x = 1$, $x = 2$, and $x = 3$ m). At each streamwise location, the two DNS profiles are nearly identical and also agree well with the RANS solution that shows some small but nonzero deviation with respect to the DNS profiles. Analogous comparisons of the Reynolds-stress profiles obtained from the two nozzle DNS solutions and a previously published flat-plate DNS are depicted in Fig. 5. The flat-plate DNS solution is from Zhang et al. [32] with $M_\infty = 5.86$ and $T_w/T_r = 0.76$. We normalize the Reynolds stresses by the Morkovin transformed velocity scale [33], which is given by $u_M = u_\tau \sqrt{\rho_w/\rho}$. There is relatively good agreement for all of the Reynolds stresses between the two nozzle DNS solutions with different grids and the flat-plate DNS solution. We computed the L_2 error between the flat-plate solution and our refined nozzle DNS solution, and we found it to be less than 20% for every Reynolds-stress component (similar result with baseline grid). Figures 2–5 show that the hydrodynamic characteristics of the TBLs remain unchanged between the baseline and refined DNS solutions.

After confirming that the basic flow characteristics based on the two DNS solutions match each other and the RANS data, as well as in some cases with previously published DNS of a flat-plate boundary layer at a similar Mach number, we performed a few more analyses that allow us to evaluate the effects of the pressure gradient, wall temperature, and freestream density. In addition to the Reynolds stresses that are shown in Fig. 5, we computed the Favre-averaged stresses. Figure 6 depicts comparisons between the wall-normal profiles of Reynolds- and Favre-averaged stresses at three selected streamwise locations ($x = 1.5$, $x = 2.5$, and $x = 3.5$ m). We see that the Reynolds- and Favre-averaged stresses are similar to one another, both in the boundary layer and in the freestream region. The largest differences between the boundary-layer profiles based on the two types of averaging are observed within the boundary-layer region and for the Reynolds shear stresses. These differences become much smaller with increasing distance from the bottom nozzle wall at $z_n/\delta = 0$.

Next, we plot the van Driest transformed mean velocity u^+_{VD} vs z^+ in Fig. 7 from a quasi-2-D nozzle DNS solution with the refined grid described in Sec. II and several flat-plate calculations [13,14,34] at similar freestream Mach numbers. The van Driest transformed mean velocity is defined as the following:

$$u^+_{\mathrm{VD}} = \int_0^{u^+} (\rho/\rho_w)^{1/2}\, \mathrm{d}u^+ \tag{2}$$

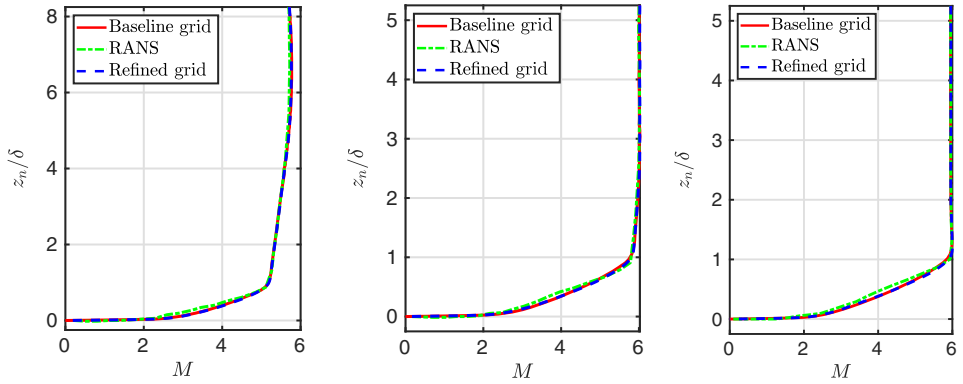

a) Profile at x = 1 m b) Profile at x = 2 m c) Profile at x = 3 m

Fig. 4 Boundary-layer profile comparisons at a) $x = 1$, b) $x = 2$, and c) $x = 3$ m in terms of Mach number for one RANS and two DNS solutions with different grids.

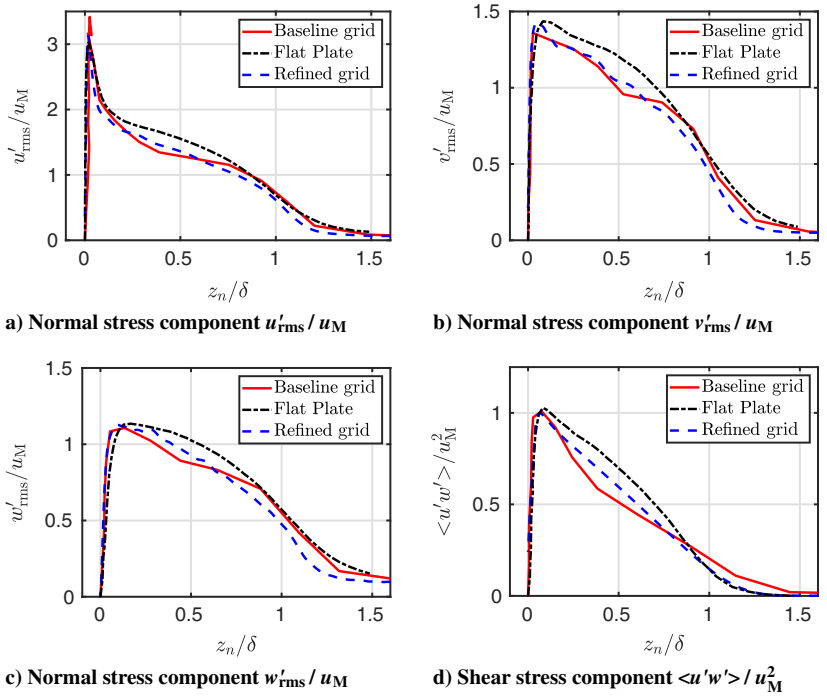

a) Normal stress component $u'_{\mathrm{rms}}/u_{\mathrm{M}}$ b) Normal stress component $v'_{\mathrm{rms}}/u_{\mathrm{M}}$

c) Normal stress component $w'_{\mathrm{rms}}/u_{\mathrm{M}}$ d) Shear stress component $<u'w'>/u_{\mathrm{M}}^2$

Fig. 5 Comparisons of the Reynolds stresses in the wall-normal direction at $x = 3.3$ m for a $M_\infty = 5.86$ and $T_w/T_r = 0.76$ flat-plate DNS solution from Zhang et al. [32] and two nozzle DNS solutions with different grids.

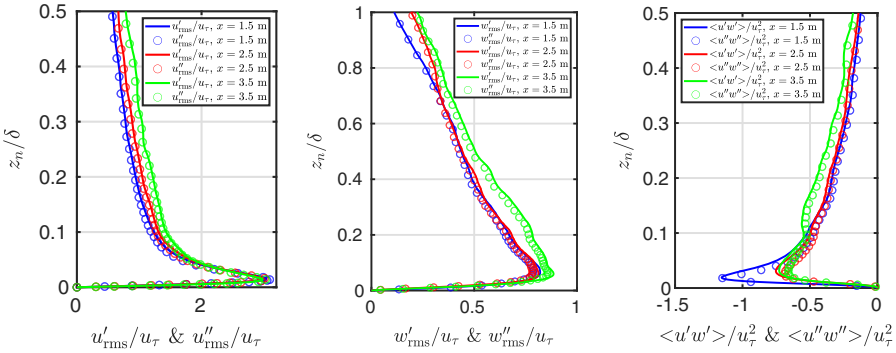

a) Streamwise normal stresses b) Cross-stream normal stresses c) Shear stresses

Fig. 6 Comparisons of the Favre-averaged q'' and Reynolds-averaged q' profiles of the normal and shear stresses at $x = 1.5$, $x = 2.5$, and $x = 3.5$ m; results are based on the refined quasi-2-D nozzle DNS solution.

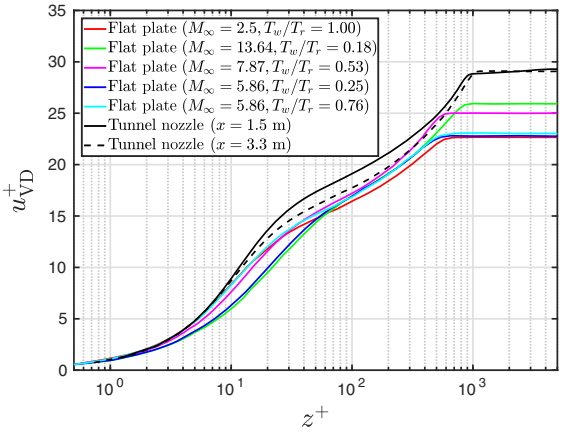

Fig. 7 van Driest transformation [35] applied to mean velocity profiles from the refined nozzle DNS and various flat-plate calculations [13,14,34], adapted from Zhang et al. [32].

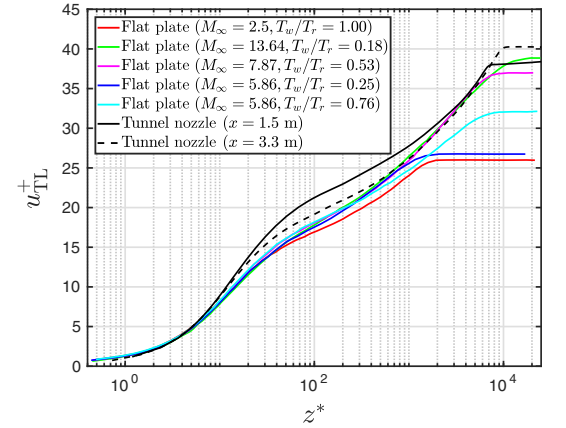

Fig. 8 Trettel and Larsson transformation [36] applied to mean velocity profiles from the refined nozzle DNS and various flat-plate calculations [13,14,34], adapted from Zhang et al. [32].

where $u^+ = \bar{u}/u_\tau$ from [35]. We see that in Fig. 7, the different slopes of the u^+_{VD} profiles for the tunnel nozzle and flat-plate cases agree quite well in the linear viscous sublayer and in the log layer. However, the values of u^+_{VD} in the boundary-layer region are larger for the nozzle simulations than for the various flat-plate cases. This is because the Reynolds number based on the shear velocity and the wall viscosity, Re_τ, is greater in our nozzle simulation than in the other cases that are considered in Fig. 7.

In addition to the van Driest transformation, we perform an alternative transformation of the mean velocity, as proposed by Trettel and Larsson [36], wherein the velocity scaling is defined below

$$u^+_{\mathrm{TL}} = \int_0^{u^+} \left(\frac{\rho}{\rho_w}\right)^{1/2} \left[1 + \frac{1}{2\rho}\frac{d\rho}{dz}z - \frac{1}{\mu}\frac{d\mu}{dz}z\right] \mathrm{d}u^+ \tag{3}$$

We plot u^+_{TL} vs z^* in Fig. 8, where $z^* = \rho z(\tau_w/\rho)^{1/2}/\mu$ from [37]. Figure 8 includes results from a quasi-2-D nozzle DNS solution with the refined grid described in Sec. II and several flat-plate calculations [13,14,34] at similar freestream Mach numbers. The flat-plate data in both Figs. 7 and 8 have been adapted from an earlier work by Zhang et al. [32]. When compared to the van Driest transformation considered earlier, the transformation by Trettel and Larsson [36] shows an improved collapse of the nozzle and flat-plate data within the viscous sublayer region. This improved collapse is expected because the Trettel and Larsson transformation is designed to satisfy the stress-balance condition within the inner layer. Notice that the collapse within the log region is not as good as that in the near-wall region, and the extent of agreement between the profiles transformed with the Trettel and Larsson transformation is comparable to that obtained with the van Driest transformation. Figures 5, 7, and 8 all depict generally decent comparisons between the nozzle and flat-plate data when the appropriate transformation has been applied.

High-order statistics of the fluctuating flow are considered next to analyze the spatial structure of the radiated acoustic field. While the fourth-order moments were not adequately converged within the current duration of the DNS, statistically converged results were obtained for the third-order moments (i.e., the skewness profiles). Figures 9a–9c depict the temperature, pressure, and density skewness profiles from the DNS solution of the quasi-2-D nozzle obtained with the refined grid described in Sec. II. These calculations are performed at $x = 3.3$ m by using 150 instantaneous snapshots. The temperature skewness is defined as $\langle T'^3\rangle/\langle T^2\rangle^{3/2}$, the pressure skewness is defined as $\langle p'^3\rangle/\langle p^2\rangle^{3/2}$, and the density skewness is defined as $\langle \rho'^3\rangle/\langle \rho^2\rangle^{3/2}$. All three skewness profiles in Fig. 9 are quite smooth and symmetric with respect to the nozzle centerline, indicating good convergence of the third-order statistical moments. Similar predictions obtained with two-thirds of the sampling interval indicated good agreement with the data shown here, providing further confidence that the results are statistically converged (see Ref. [21]).

The wall-normal profile of the temperature skewness in Fig. 9a exhibits two large positive peaks, one each near the boundary-layer edge along either wall. The skewness is nearly uniform within the freestream region, with a relatively small but positive value of approximately 0.3 within the nozzle core. Figure 9b shows that the skewness profiles for the fluctuations in all three thermodynamic variables are nearly uniform within the freestream region and, furthermore, nearly overlap with each other. This finding further supports the spatial homogeneity of the radiated acoustic field in spite of

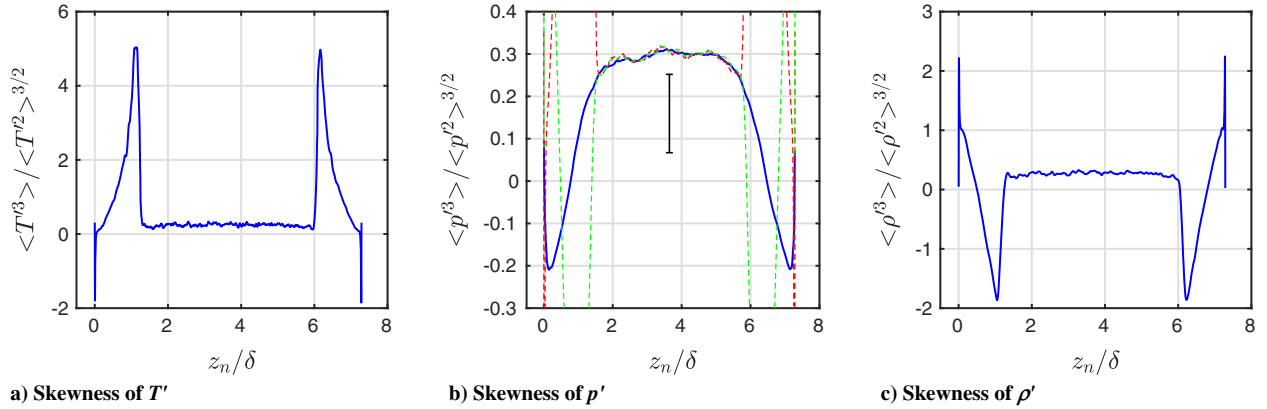

a) Skewness of T' **b) Skewness of p'** **c) Skewness of ρ'**

Fig. 9 Skewness of the temperature, pressure, and density fluctuations at $x = 3.3$ m from the refined quasi-2-D DNS; the red and green dashed lines in the middle plot are the temperature and density skewness, respectively. The black line represents the skewness range from experiments [19].

the nozzle wall at either end of the wall-normal domain. We also show the skewness from experimental measurements of the pitot pressure fluctuations made in the NASA 20-Inch Mach 6 Wind Tunnel [19] at unit $Re = 6.4 \times 10^6$ (1/m) in Fig. 9b. Note that unit $Re = 6.4 \times 10^6$ (1/m) is slightly different than unit $Re = 7.3 \times 10^6$ (1/m) for our simulations. Figure 9c indicates that the density skewness has two large negative peaks near the boundary-layer edges that approximately coincide with the positive peaks in the skewness profile of the temperature fluctuations. On the other hand, negative peaks in the pressure skewness profiles occur relatively close to the nozzle walls. The inverse relation between the temperature and density fluctuations is anticipated because of the equation of state for a perfect gas, because the pressure fluctuations are not expected to become large enough to support fluctuations of the same sign in both the temperature and density.

Figure 10 shows that despite the presence of more visible oscillations in the kurtosis profile (defined as $\langle p'^4 \rangle / \langle p^2 \rangle^2$) for pressure fluctuations within the freestream region, the mean kurtosis indicates a relatively small deviation from the Gaussian behavior (i.e., change of 0.2 from roughly 3.2). Thus, the single-point statistics up to fourth-order moments are strongly suggestive of nearly Gaussian acoustic pressure fluctuations within the nozzle core. This finding has significant implications for reduced-order modeling (i.e., synthesis) of the radiated acoustic field, as the Gaussian behavior would imply that the more easily computable or measurable statistics up to second order is nearly sufficient for a complete characterization of the stochastic radiation field. We also show the kurtosis from experimental measurements of the pitot pressure fluctuations made in the NASA 20-Inch Mach 6 Wind Tunnel [19] at unit $Re = 6.4 \times 10^6$ (1/m) in Fig. 10. Even though our simulation is quasi-2-D (not fully 3-D)

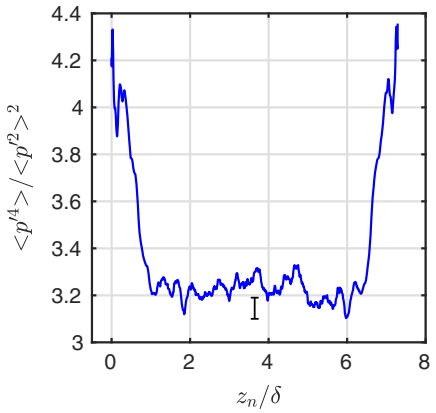

Fig. 10 Kurtosis of the pressure fluctuations at $x = 3.3$ m from the refined quasi-2-D DNS; the black line represents the kurtosis range from experiments [19].

and at a slightly different Reynolds number, we obtain relatively good agreement with experiments.

B. Pressure Fluctuations

Because we have established that the hydrodynamic characteristics of the TBL remain virtually unchanged between the two DNS solutions with different grids, we now compare the associated pressure fluctuations, both within the boundary layer and inside the nozzle core (i.e., freestream) regions. Figure 11 shows the wall-normal variation of the rms pressure fluctuation field divided by the freestream pressure for two quasi-2-D nozzle DNS solutions with different grids at three streamwise locations. We see from Fig. 11 that the baseline and refined DNS solutions have small oscillations in the pressure fluctuation profiles, but the overall trends of the profiles are quite similar. In general, the pressure fluctuation profile is nearly uniform beyond a distance of approximately 2δ away from each tunnel nozzle wall.

Figure 12 depicts the power spectral density (PSD) of the freestream acoustic fluctuations vs the frequency taken from a circular-nozzle DNS [14] of the Hypersonic Ludwieg Tube Braunschweig (HLB), a flat-plate DNS [34] of the Purdue Boeing/U.S. Air Force Office of Scientific Research Mach-6 Quiet Tunnel (BAM6QT), and two rectangular-nozzle quasi-2-D DNS with different grids. For the quasi-2-D nozzle cases, the PSD is computed about $z = 0$ and $x = 3.3$ m. There is relatively good agreement between all of the DNS solutions. All of the nozzle cases have oscillations at smaller frequencies, while the flat-plate case is very smooth. This is most likely due to the overall run time of the simulations. We can see in Fig. 12 that the rectangular-nozzle PSD and the circular-nozzle PSD agree well at larger frequencies.

The frequency content of the freestream fluctuations in Fig. 12 is similar for every case. We plot the bulk propagation speed U_b of the pressure fluctuations as a function of wall-normal distance at $x = 3.3$ m in Fig. 13. The minimum value of the real-time evolution of $p(x, t)$ subtracted by a frozen wave approximated by $p(x - U_b t)$ is generally defined as the bulk propagation speed. We use the following expression to calculate the bulk propagation speed in terms of time-averaged partial derivatives of the pressure:

$$U_b = -\frac{\overline{(\partial p/\partial t)(\partial p/\partial x)}}{\overline{(\partial p/\partial x)^2}} \tag{4}$$

The wall-normal variation in U_b is similar for every configuration in Fig. 13. However, the advection speeds in the flat-plate and circular-nozzle cases reach larger values within the outer part of the boundary layer than those estimated for the quasi-2-D nozzle. Each case levels out to $U_b \approx 0.7U_\infty$ in the freestream. Both of the quasi-2-D nozzle cases agree with each other, but the refined grid yields a smoother distribution. The bulk propagation speed of $U_b \approx 0.7U_\infty$ corresponds to slow acoustic disturbances that propagate at a relative

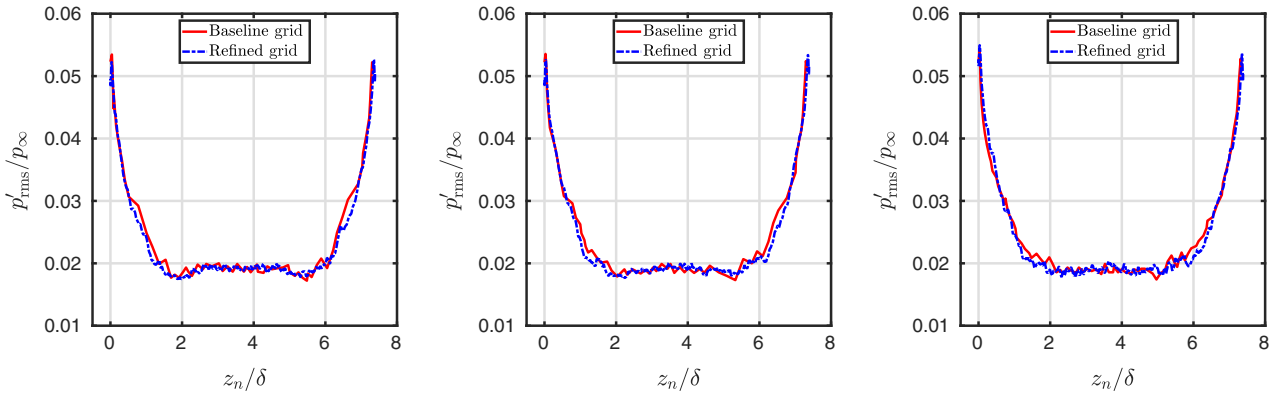

a) Profile at $x = 3.3$ m **b) Profile at $x = 3.4$ m** **c) Profile at $x = 3.5$ m**

Fig. 11 Comparisons of the wall-normal variation of the rms pressure fluctuations at a) $x = 3.3$, b) $x = 3.4$, and c) $x = 3.5$ m between two quasi-2-D DNS solutions with different grids.

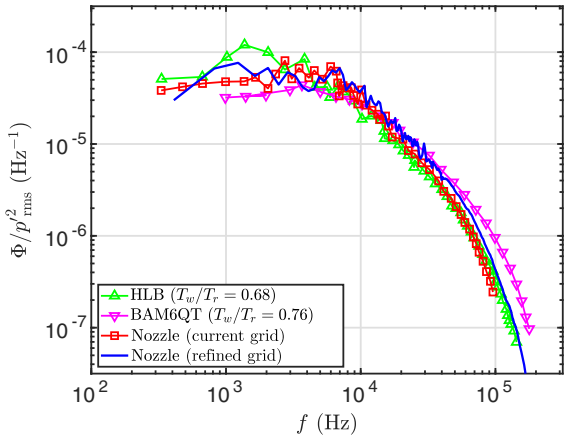

Fig. 12 PSD of acoustic fluctuations vs frequency taken from a circular-nozzle DNS [14], a flat-plate DNS [34], and two rectangular-nozzle quasi-2-D DNS with different grids (computed about $z = 0$ and $x = 3.3$ m).

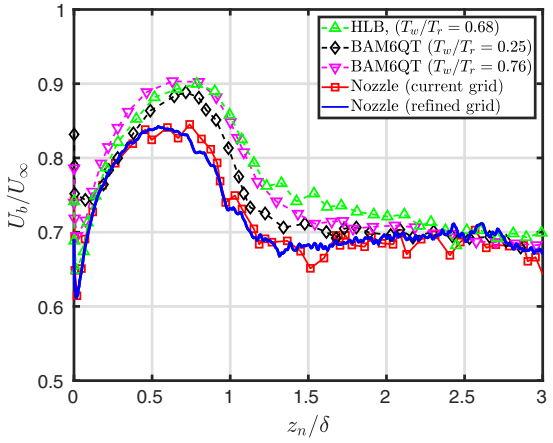

Fig. 13 Bulk propagation speed of freestream acoustic fluctuations taken from a circular-nozzle DNS [14], two flat-plate DNS [34], and two rectangular-nozzle quasi-2-D DNS with different grids (computed about $x = 3.3$ m).

Mach number of nearly 1.8 with respect to the mean centerline velocity. Earlier DNS of a Mach 5.86 TBL over a flat plate by Duan et al. [13] had shown that disturbances with slow phase speeds dominate the radiated acoustic field. They used multiple techniques to characterize the bulk propagation speed, and they all indicated the dominance of slow acoustic disturbances with phase speeds less than the local freestream speed. The data retained from the present simulation were not sufficient to provide a reliable characterization of the phase velocity distribution in a rectangular-nozzle test section; however, similar results as the flat-plate case may be expected on the basis of the other similarities in acoustic radiation with the simulations from Ref. [13] (Figs. 12 and 13). It may be noted that the estimation of bulk propagation speed does not preclude the existence of fast acoustic disturbances within a limited range of frequencies, and a more in-depth analysis of the spatiotemporal spectrum would be necessary to establish that no significant fast acoustic disturbances are likely to be encountered within the nozzle core. This exercise is deferred to a future investigation.

To visualize the 3-D flowfield of the rectangular tunnel nozzle DNS solution with two spatially evolving TBLs, we plot an instantaneous snapshot with color contours of Q-criterion isosurfaces and grayscale contours of density gradient magnitude (DGM) in Fig. 14. The spatial development of the two boundary layers can be seen in the Q-criterion isosurfaces. Notice that both TBLs grow at approximately the same rate. Grayscale contours of the DGM on an xz plane from the DNS with two TBLs are shown in Fig. 15a. Acoustic fluctuations radiating from both TBLs at angles ranging from roughly

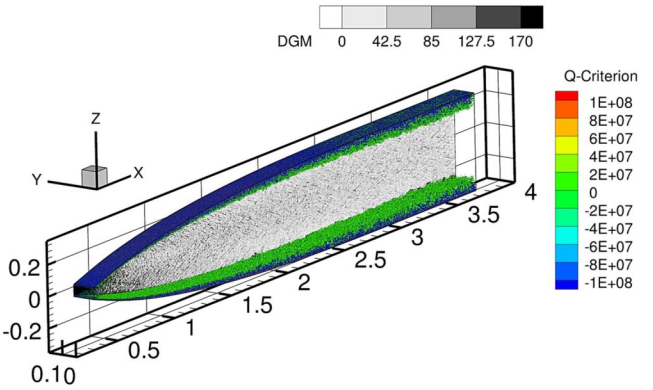

Fig. 14 Instantaneous snapshot with color contours of Q-criterion isosurfaces and grayscale contours of DGM from the refined quasi-2-D DNS; the nozzle shape has been nonuniformly distorted.

30 to 35 deg can be seen in the grayscale contours of the DGM (see also Deegan et al. [20]). Figure 15b shows grayscale contours of the DGM on a yz plane from the DNS with two TBLs at $x = 1.6$ m. Notice in Fig. 15b that both TBLs are radiating acoustics in the spanwise direction.

Along with running quasi-2-D nozzle simulations that have two spatially developing TBLs, we also performed a simulation that has just one TBL developing on the bottom wall. This simulation will be used to compare against the DNS with both TBLs to isolate the influence of individual TBLs on freestream acoustic disturbances. Moreover, the simulation with one TBL on the bottom wall employs a turbulent RANS solution that has no correlation random fluctuations added from the digital-filter-based synthetic injection method for the top boundary layer at the inflow station. We use a no-slip boundary condition along the upper nozzle wall. Hence, the top boundary layer does not represent a laminar solution over a tunnel wall, but mainly a flow that does not propagate noise unless and until it transitions (much farther downstream of the inflow region) due to the excitation of instabilities via the acoustic radiation from the bottom wall. Grayscale contours of the DGM on a streamwise wall-normal plane from the DNS with a single TBL are depicted in Fig. 16a. Notice in Fig. 16a that acoustic waves radiate from the bottom wall and not the top wall. This differs from Fig. 15a, which shows acoustic fluctuations radiating from both walls due to the turbulence that is generated by the top and bottom TBLs. Hence, the acoustic waves form a symmetric cross shape in Fig. 15a, whereas in Fig. 16a the acoustic waves only propagate in one direction. We show grayscale contours of the DGM on a yz plane from the DNS with a single TBL at $x = 1.6$ m in Fig. 16b so that one can see that the spanwise distribution of the acoustics upstream for this case is only near the bottom wall.

The rms pressure fluctuation field divided by the wall shear stress induced by the TBL over the bottom nozzle wall is plotted in Fig. 17 for three quasi-2-D nozzle simulations, two separate flat-plate DNS solutions [34], and a circular-nozzle solution [14] at similar freestream Mach numbers. We see that the values of $p_{\rm rms}/\tau_w$ vs z_n from the nozzle DNS that has just one TBL agree better with the flat-plate calculations [13,34]. This result is expected because the flat-plate simulations have just one TBL by definition. The nozzle simulation with two TBLs and the refined grid is similar to the corresponding result with the baseline grid, indicating the insensitivity of noise characteristics in the test section to the mesh resolution. Furthermore, the value of $p'_{\rm rms}/\tau_w$ in the freestream is larger by a factor of approximately 1.3 for the case with TBLs developing along both nozzle walls than in an unconfined acoustic environment. The fact that this ratio is relatively close to $\sqrt{2}$ suggests the acoustic intensity at $x = 3.3$ m is nearly equivalent to the superposition of acoustic radiation from two identical but statistically independent source fields near the top and bottom walls, respectively. In other words, the effects of acoustic reverberation appear to be relatively weak at this location.

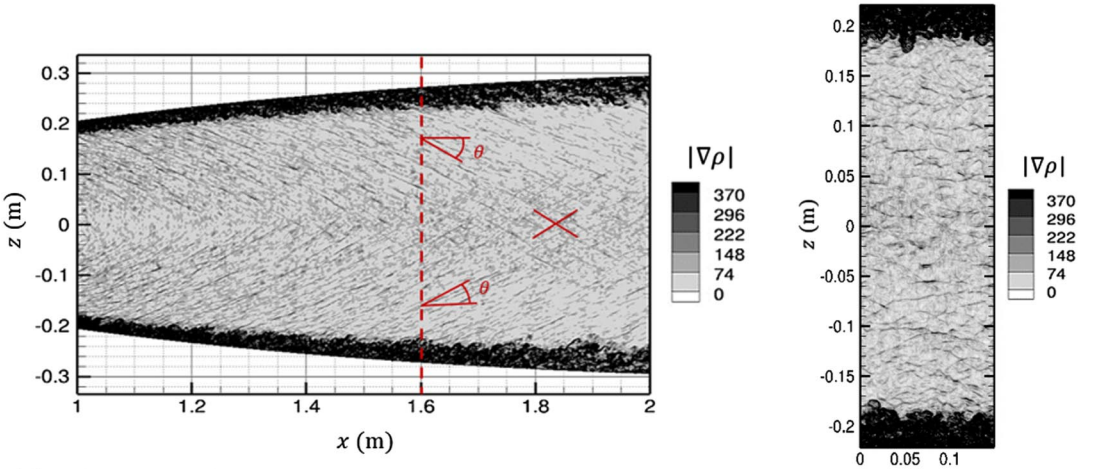

a) Snapshot on an xz plane

b) Snapshot on a yz plane at $x = 1.6$ m

Fig. 15 Instantaneous snapshot with grayscale contours of DGM on both an a) xz plane and a b) yz plane from the refined quasi-2-D DNS with both TBLs; the nozzle shape has been nonuniformly distorted.

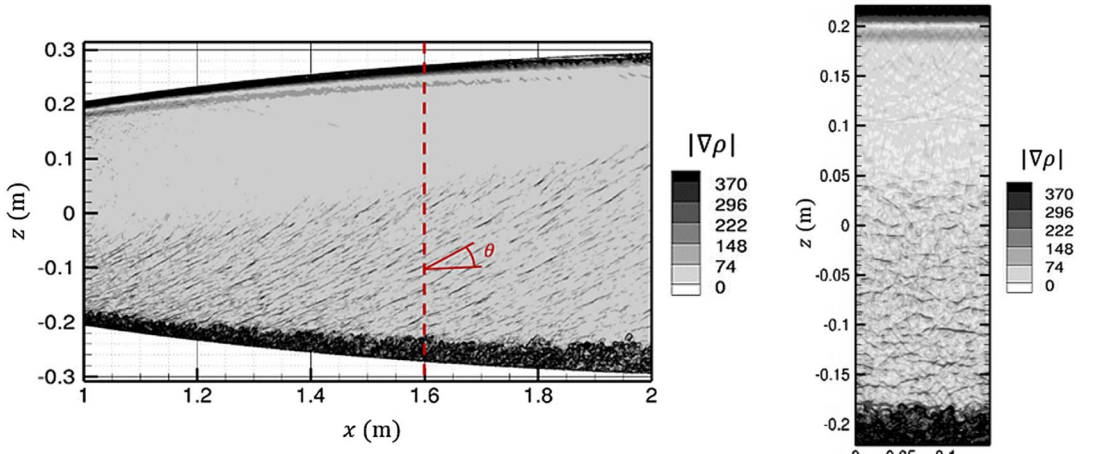

a) Snapshot on an xz plane

b) Snapshot on a yz plane at $x = 1.6$ m

Fig. 16 Instantaneous snapshot with grayscale contours of DGM on both an a) xz plane and a b) yz plane from the refined quasi-2-D DNS with one TBL; the nozzle shape has been nonuniformly distorted.

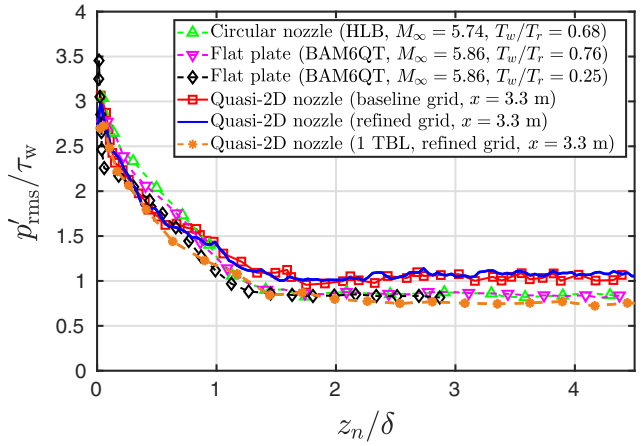

Fig. 17 Comparison of p'_{rms}/τ_w induced by the lower TBL between three rectangular-nozzle quasi-2-D DNS at $x = 3.3$ m, a circular-nozzle DNS [14], and two flat-plate DNS [34].

We define the two-point correlation coefficient in the xz plane as the following:

$$C_{\mathrm{pp}}(\Delta x, z, z_{\mathrm{ref}}) = \frac{\overline{p'(x, y, z_{\mathrm{ref}}, t)p'(x + \Delta x, y, z, t)}}{[\overline{p'^2(x, y, z_{\mathrm{ref}}, t)}]^{1/2}[\overline{p'^2(x + \Delta x, y, z, t)}]^{1/2}} \quad (5)$$

where Δx represents the spatial separation in the streamwise direction, and z_{ref} is the reference wall-normal location at which the correlation is computed. Figure 18a shows the two-point correlation coefficient of the pressure signal at four wall-normal positions, which include $z_{\mathrm{ref}} = -0.251, -0.138, -0.0689$, and 0 m, from the refined quasi-2-D DNS solution with two TBLs. Here, the four wall-normal positions also correspond to $z/\delta = -3.64, -2, -1$, and 0. The correlation coefficients in Fig. 18 are computed at a streamwise location of $x = 3.3$ m. Figure 18b depicts the two-point correlation coefficient of the pressure signal at the same four wall-normal positions in Fig. 18a, but from the refined quasi-2-D DNS solution with a single TBL instead of two.

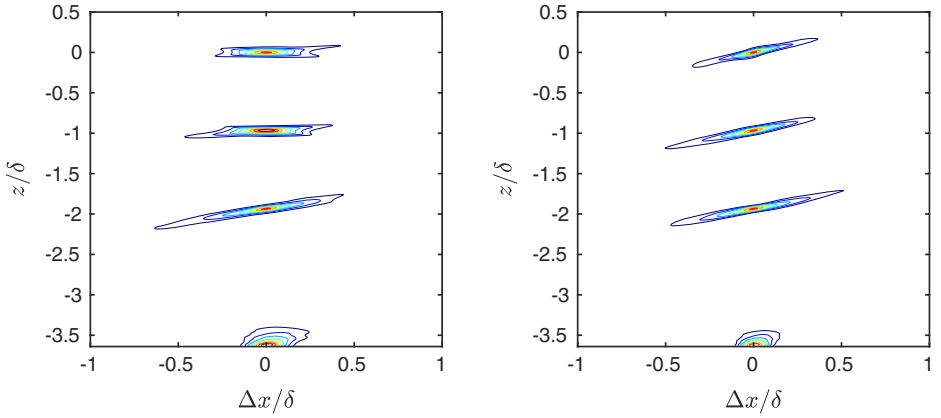

a) DNS with two turbulent boundary layers **b) DNS with one turbulent boundary layer**

Fig. 18 Contours of $C_{pp}(\Delta x, z, z_{ref})$ about the pressure signal at $x = 3.3$ m and multiple wall-normal positions from the refined quasi-2-D DNS; contour levels vary from 0.2 (blue) to 0.9 (red) with increments of 0.1.

At the bottom nozzle wall ($z_{ref} = -0.251$ m), the correlation contours have a structure that is almost perpendicular to the wall. Notice that the overall shape of the near-wall correlation contours is similar for a single TBL (Fig. 18b) and for the case with two TBLs (Fig. 18a). However, differences between the correlation contours in these two cases become apparent for reference locations within the local freestream region ($z_{ref} = -0.0689$ and 0 m). The correlation contours for the case with a single TBL are inclined upward for $\Delta x > 0$, analogous to the previous computations for a flat-plate boundary layer [32]. The correlation contours for the case with both TBLs are inclined similarly for $z_{ref} = -0.138$ m ($z/\delta = -2$) (i.e., approximately where the rms pressure fluctuations asymptote to their freestream value in Fig. 17). The presence of upward inclined contours in this case indicates a dominance of the acoustic field radiation from the bottom wall in the lower half of the nozzle, which is corroborated by the DGM contours in Fig. 15a. Acoustic disturbances arise from turbulent eddies in a high-speed boundary layer. The radiation of acoustic waves in our simulation is explained via the classic theory of Mach wave radiation and experimental measurements by Laufer [5]. Mach waves are defined as shocks caused by the supersonic movement of turbulent eddies with respect to the surrounding flow that radiate noise. Farther beyond the wall-normal location of $z/\delta = -2$, the correlation contours in Fig. 18a begin to show a weak but visible component that corresponds to downward inclined contours for $\Delta x > 0$. As a result of the superposition of comparable contributions from the acoustic sources in both TBLs, the correlation contours tend to flatten as z_{ref} approaches the nozzle centerline. Indeed, as a result of the statistical symmetry in this configuration, the correlation contours along the centerline ($z_{ref} = 0$) are roughly symmetric with respect to the wall-normal coordinate, with minor deviations from a symmetric behavior indicating the lack of full statistical convergence.

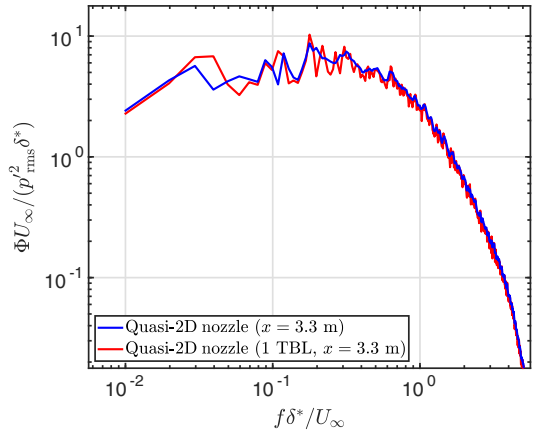

Fig. 19 PSD of surface pressure fluctuations at the bottom wall computed about $x = 3.3$ m vs nondimensional frequency taken from two quasi-2-D DNS with either one TBL or two.

To further characterize the impact of an additional fully TBL on the nozzle acoustics, we compare the pressure fluctuations along the bottom wall between the one and two turbulent boundary-layer cases in Fig. 19. Oscillations in the PSD are more apparent in the one TBL case because it has a slightly smaller run time. However, the PSD of surface pressure fluctuations happens to be fairly similar along the bottom wall between the two different cases, which signifies that the incoming freestream disturbances from the opposite wall have a negligible influence on the intensity of surface pressure fluctuations along the nozzle walls. This can also be seen in Fig. 18 by comparing the two-point correlation coefficient of the pressure signal between the two different cases at $z_{ref} = -0.251$ m.

V. Conclusions

With the goal of contributing to an improved understanding of the wind-tunnel acoustic environment in nonaxisymmetric test sections, the preliminary computations by Deegan et al. [20] and Hildebrand et al. [21] have been extended to report on the DNS of acoustic radiation from the TBLs on the walls of a quasi-2-D rectangular nozzle. Comparisons of the centerline Mach number, boundary-layer thickness, Reynolds stresses, boundary-layer profiles, and rms pressure fluctuation fields between the simulations based on two different mesh resolutions indicated good agreement, confirming that the computed turbulence and noise characteristics are practically insensitive to the mesh resolution used in this work. The Reynolds- and Favre-averaged stresses at three different streamwise locations along the nozzle were also compared, indicating a similar flow behavior among these stations, both inside and outside the boundary layer. Furthermore, an application of the compressibility transformations by van Driest [35] along with Trettel and Larsson [36] enabled a successful comparison between the present nozzle computation and previous flat-plate data for different Mach numbers and wall-cooling ratios.

By suppressing the effects of the spanwise end walls and the corners on the acoustic noise generation, the simpler quasi-2-D flow configuration proved useful in characterizing the effects of the individual wind-tunnel walls on the acoustic disturbance field inside the test section. The most notable findings of this work are enumerated as follows:

1) Freestream fluctuations in all thermodynamic variables have a skewness of approximately 0.3, and the kurtosis of the pressure fluctuations is approximately 3.2, indicating small deviations with respect to the corresponding moments of a Gaussian field.

2) The normalized frequency spectra of the freestream acoustic disturbances in the different nozzle and flat-plate cases agree well with each other, except at very low frequencies.

3) The scaled value of the freestream acoustic pressure fluctuation, p'_{rms}/τ_w, for the 2-D nozzle with TBLs along both walls is significantly higher than that in an unconfined acoustic environment, with the relative increase in p'_{rms}/τ_w corresponding to a factor of nearly $\sqrt{2}$.

4) Pressure correlation contours in the streamwise wall-normal plane clearly indicate the dual origin of the acoustic field within a given cross section of the nozzle with TBLs along each wall.

5) The surface pressure fluctuations along the nozzle walls are not significantly influenced by the presence of the opposite nozzle wall or the acoustic disturbances emanating from that wall.

Future work will focus on the effects that both spanwise end walls and corners have on the acoustic noise generation and reverberation processes in a rectangular nozzle test section. This will include comparisons with the present DNS and experimental measurements performed in the NASA 20-Inch Mach 6 Wind Tunnel.

Acknowledgments

This work was performed as part of the Hypersonic Technology Project of the NASA Advanced Air Vehicles Program. The authors (Cole P. Deegan, Junji Huang, and Lian Duan) would like to acknowledge financial support by the Office of Naval Research under grant N00014-17-1-2347, managed by Eric Marineau. Computational resources supporting this work are provided by the NASA High-End Computing program through the NASA Advanced Supercomputing Division at NASA Ames Research Center. Furthermore, the authors would like to thank Jeffery White and Robert Baurle of the NASA Langley Research Center for their assistance with the Reynolds-averaged Navier–Stokes computations. Lastly, the authors want to thank Amanda Chou for her excellent comments and for providing skewness and kurtosis data from experiments in the NASA 20-Inch Mach 6 Wind Tunnel.

References

[1] Kimmel, R., "Aspects of Hypersonic Boundary Layer Transition Control," AIAA Paper 2003-0772, Jan. 2003. https://doi.org/10.2514/6.2003-772

[2] Schneider, S. P., "Effects of High-Speed Tunnel Noise on Laminar-Turbulent Transition," *Journal of Spacecraft and Rockets*, Vol. 38, No. 3, 2001, pp. 323–333. https://doi.org/10.2514/2.3705

[3] Morkovin, M. V., "On Transition Experiments at Moderate Supersonic Speeds," *Journal of the Aeronautical Sciences*, Vol. 24, No. 7, 1957, pp. 480–486. https://doi.org/10.2514/8.3887

[4] Laufer, J., "Aerodynamic Noise in Supersonic Wind Tunnels," *Journal of the Aeronautical Sciences*, Vol. 28, No. 9, 1961, pp. 685–692. https://doi.org/10.2514/8.9150

[5] Laufer, J., "Some Statistical Properties of the Pressure Field Radiated by a Turbulent Boundary Layer," *Physics of Fluids*, Vol. 7, No. 8, 1964, pp. 1191–1197. https://doi.org/10.1063/1.1711360

[6] Pate, S. R., "Measurements and Correlations of Transition Reynolds Numbers on Sharp Slender Cones at High Speeds," *AIAA Journal*, Vol. 9, No. 6, 1971, pp. 1082–1090. https://doi.org/10.2514/3.49919

[7] Stetson, K. F., "Nosetip Bluntness Effects on Cone Frustum Boundary-Layer Transition in Hypersonic Flow," AIAA Paper 1983-1763, July 1983. https://doi.org/10.2514/6.1983-1763

[8] Fedorov, A. V., "Receptivity of a High-Speed Boundary Layer to Acoustic Disturbances," *Journal of Fluid Mechanics*, Vol. 491, Sept. 2003, pp. 101–129. https://doi.org/10.1017/S0022112003005263

[9] Zhong, X., and Wang, X., "Direct Numerical Simulation on the Receptivity, Instability, and Transition of Hypersonic Boundary Layers," *Annual Review of Fluid Mechanics*, Vol. 44, Jan. 2012, pp. 527–561. https://doi.org/10.1146/annurev-fluid-120710-101208

[10] Donaldson, J., and Coulter, S., "A Review of Free-Stream Flow Fluctuation and Steady-State Flow Quality Measurements in the AEDC/VKF Supersonic Tunnel A and Hypersonic Tunnel B," AIAA Paper 1995-6137, April 1995. https://doi.org/10.2514/6.1995-6137

[11] Duan, L., Choudhari, M. M., and Wu, M., "Numerical Study of Acoustic Radiation Due to a Supersonic Turbulent Boundary Layer," *Journal of Fluid Mechanics*, Vol. 746, May 2014, pp. 165–192. https://doi.org/10.1017/jfm.2014.116

[12] Duan, L., and Choudhari, M. M., "Analysis of Numerical Simulation Database for Pressure Fluctuations Induced by High-Speed Turbulent Boundary Layers," AIAA Paper 2014-2912, June 2014. https://doi.org/10.2514/6.2014-2912

[13] Duan, L., Choudhari, M. M., and Zhang, C., "Pressure Fluctuations Induced by a Hypersonic Turbulent Boundary Layer," *Journal of Fluid Mechanics*, Vol. 804, Oct. 2016, pp. 578–607. https://doi.org/10.1017/jfm.2016.548

[14] Duan, L., Choudhari, M. M., Chou, A., Munoz, F., Ali, S. R. C., Radespiel, R., Schilden, T., Schröder, W., Marineau, E. C., Casper, K. M., Chaudhry, R. S., Candler, G. V., Gray, K. A., and Schneider, S. P., "Characterization of Freestream Disturbances in Conventional Hypersonic Wind Tunnels," *Journal of Spacecraft and Rockets*, Vol. 56, No. 2, 2019, pp. 357–368. https://doi.org/10.2514/1.A34290

[15] Duan, L., Nicholson, G. L., Huang, J., Casper, K. M., Wagnild, R. M., and Bitter, N. P., "Direct Numerical Simulation of Nozzle-Wall Pressure Fluctuations in a Mach 8 Wind Tunnel," AIAA Paper 2019-0874, Jan. 2019. https://doi.org/10.2514/6.2019-0874

[16] Zhang, C., and Duan, L., "Acoustic Radiation from High-Speed Turbulent Boundary Layers in a Tunnel-Like Environment," AIAA Paper 2015-0836, Jan. 2015. https://doi.org/10.2514/6.2015-0836

[17] Prasad, C., Huang, J., Duan, L., and Gaitonde, D. V., "On the Nature of Freestream Disturbances in a Two-Dimensional Supersonic Test Section," AIAA Paper 2021-0162, Jan. 2021. https://doi.org/10.2514/6.2021-0162

[18] Nicholson, G. L., Duan, L., Choudhari, M. M., and Bowersox, R. D. W., "Simulation and Modeling of Hypersonic Turbulent Boundary Layers Subject to Favorable Pressure Gradients due to Streamline Curvature," AIAA Paper 2021-1672, Jan. 2021. https://doi.org/10.2514/6.2021-1672

[19] Chou, A., Leidy, A., King, R. A., Bathel, B. F., and Herring, G., "Measurements of Freestream Fluctuations in the NASA Langley 20-Inch Mach 6 Tunnel," AIAA Paper 2018-3073, June 2018. https://doi.org/10.2514/6.2018-3073

[20] Deegan, C. P., Duan, L., and Choudhari, M. M., "Direct Numerical Simulation of Acoustic Disturbances in the Rectangular Test Section of a Hypersonic Wind Tunnel," AIAA Paper 2018-3219, June 2018. https://doi.org/10.2514/6.2020-0587

[21] Hildebrand, N., Choudhari, M. M., and Duan, L., "Direct Numerical Simulations of Acoustic Disturbances in Various Rectangular Nozzle Configurations," AIAA Paper 2020-0587, Jan. 2020. https://doi.org/10.2514/6.2020-0587

[22] Litton, D., Edwards, J., and White, J., "Algorithmic Enhancements to the VULCAN Navier-Stokes Solver," AIAA Paper 2003-3979, June 2003. https://doi.org/10.2514/6.2003-3979

[23] Menter, F. R., "Two-Equation Eddy-Viscosity Turbulence Models for Engineering Applications," *AIAA Journal*, Vol. 32, No. 8, 1994, pp. 1598–1605. https://doi.org/10.2514/3.12149

[24] Edwards, J. R., "A Low-Diffusion Flux-Splitting Scheme for Navier-Stokes Calculations," *Computers & Fluids*, Vol. 26, No. 6, July 1997, pp. 635–659. https://doi.org/10.1016/S0045-7930(97)00014-5

[25] Taylor, E. M., Wu, M., and Martín, M. P., "Optimization of Nonlinear Error Sources for Weighted Essentially Non-Oscillatory Methods in Direct Numerical Simulations of Compressible Turbulence," *Journal of Computational Physics*, Vol. 223, No. 1, 2006, pp. 384–397. https://doi.org/10.1016/j.jcp.2006.09.010

[26] Williamson, J. H., "Low-Storage Runge-Kutta Schemes," *Journal of Computational Physics*, Vol. 35, No. 1, 1980, pp. 48–56. https://doi.org/10.1016/0021-9991(80)90033-9

[27] Wu, M., and Martín, M. P., "Direct Numerical Simulation of Supersonic Turbulent Boundary Layer over a Compression Ramp," *AIAA Journal*, Vol. 45, No. 4, 2007, pp. 879–889. https://doi.org/10.2514/1.27021

[28] Touber, E., and Sandham, N. D., "Oblique Shock Impinging on a Turbulent Boundary Layer: Low-Frequency Mechanisms," AIAA Paper 2008-4170, June 2008. https://doi.org/10.2514/6.2008-4170

[29] Dhamankar, N. S., Martha, C. S., Situ, Y., Aikens, K. M., Blaisdell, G. A., Lyrintzis, A. S., and Li, Z., "Digital Filter-Based Turbulent Inflow Generation for Jet Aeroacoustics on Non-Uniform Structured Grids,"

AIAA Paper 2014-1401, Jan. 2014.
https://doi.org/10.2514/6.2014-1401

[30] Huang, J., Nicholson, G. L., Duan, L., Choudhari, M. M., and Bowersox, R. D., "Simulation and Modeling of Cold-Wall Hypersonic Turbulent Boundary Layers on Flat Plate," AIAA Paper 2020-0571, Jan. 2020.
https://doi.org/10.2514/6.2020-0571

[31] Thompson, K. W., "Time Dependent Boundary Conditions for Hyperbolic Systems," *Journal of Computational Physics*, Vol. 68, No. 1, 1987, pp. 1–24.
https://doi.org/10.1016/0021-9991(87)90041-6

[32] Zhang, C., Duan, L., and Choudhari, M. M., "Direct Numerical Simulation Database for Supersonic and Hypersonic Turbulent Boundary Layers," *AIAA Journal*, Vol. 56, No. 11, 2018, pp. 4297–4311.
https://doi.org/10.2514/1.J057296

[33] Morkovin, M. V., "Effects of Compressibility on Turbulent Flows," *Mécanique de la Turbulence*, edited by A. J. Farve, CNRS, Paris, 1962, pp. 367–380.

[34] Zhang, C., Duan, L., and Choudhari, M. M., "Effect of Wall Cooling on Boundary Layer Induced Pressure Fluctuations at Mach 6," *Journal of Fluid Mechanics*, Vol. 822, July 2017, pp. 5–30.
https://doi.org/10.1017/jfm.2017.212

[35] van Driest, E. R., "The Problem of Aerodynamic Heating," *Aeronautical Engineering Review*, Vol. 15, No. 10, 1956, pp. 26–41.

[36] Trettel, A., and Larsson, J., "Mean Velocity Scaling for Compressible Wall Turbulence with Heat Transfer," *Physics of Fluids*, Vol. 28, No. 2, 2016, Paper 026102.
https://doi.org/10.1063/1.4942022

[37] Huang, P. G., Coleman, G., and Bradshaw, P., "Compressible Turbulent Channel Flows: DNS Results and Modelling," *Journal of Fluid Mechanics*, Vol. 305, Dec. 1995, pp. 185–218.
https://doi.org/10.1017/S0022112095004599

N. D. Sandham
Associate Editor